Original Paper

Source wavefield reconstruction based on an implicit staggered-grid finite-difference operator for seismic imaging

Zhi-Ming Ren [a, b, *], Xue Dai [a], Qian-Zong Bao [a, b]

[a] Chang'an University, College of Geological Engineering and Geomatics, Xi'an, Shaanxi, 710064, China
[b] National Engineering Research Center of Offshore Oil and Gas Exploration, Beijing, 100028, China

A R T I C L E I N F O

A B S T R A C T

Reverse time migration and full waveform inversion involve the crosscorrelation of two wavefields, propagated in the forward- and reverse-time directions, respectively. As a result, the forward-propagated wavefield needs to be stored, and then accessed to compute the correlation with the backward-propagated wavefield. Boundary-value methods reconstruct the source wavefield using saved boundary wavefields and can significantly reduce the storage requirements. However, the existing boundary-value methods are based on the explicit finite-difference (FD) approximations of the spatial derivatives. Implicit FD methods exhibit greater accuracy and thus allow for a smaller operator length. We develop two (an accuracy-preserving and a memory-efficient) wavefield reconstruction schemes based on an implicit staggered-grid FD (SFD) operator. The former uses boundary wavefields at M layers of grid points and the spatial derivatives of wavefields at one layer of grid points to reconstruct the source wavefield for a $(2M+2)$th-order implicit SFD operator. The latter applies boundary wavefields at N layers of grid points, a linear combination of wavefields at $M-N$ layers of grid points, and the spatial derivatives of wavefields at one layer of grid points to reconstruct the source wavefield ($0 \leq N < M$). The required memory of accuracy-preserving and memory-efficient schemes is $(M+1)/M$ and $(N+2)/M$ times, respectively, that of the explicit reconstruction scheme. Numerical results reveal that the accuracy-preserving scheme can achieve accurate reconstruction at the cost of storage. The memory-efficient scheme with $N = 2$ can obtain plausible reconstructed wavefields and images, and the storage amount is $4/(M+1)$ of the accuracy-preserving scheme.
© 2022 The Authors. Publishing services by Elsevier B.V. on behalf of KeAi Communications Co. Ltd. This is an open access article under the CC BY-NC-ND license (http://creativecommons.org/licenses/by-nc-nd/4.0/).

1. Introduction

The adjoint-state method is commonly used in seismic imaging and inversion, such as reverse time migration (RTM) (McMechan, 1983; Zhang et al., 2007; Liu et al., 2011; Gu et al., 2019) and full waveform inversion (FWI) (Tarantola, 1984; Plessix, 2006; Virieux and Operto, 2009; Métivier et al., 2017; Zhang and Alkhalifah, 2019). The adjoint-state method requires source and receiver/adjoint wavefields, accessible at the same time to form the image condition or misfit gradient. However, the two wavefields are propagated in the forward- and reverse-time directions, respectively, Hence, the source wavefield should be stored during the

forward propagation, and then accessed during the backward propagation for multiplication with the same-step adjoint wavefield. The storage requirements can become unaffordable for large-scale problems.

To reduce the cost of storing the source wavefield, researchers have developed two types of source wavefield reconstruction methods: the optimal checkpointing method and the boundary value method. The former uses the snapshots at several points in time as an initial value to recompute the source wavefield forward in time. The latter applies saved boundary wavefields and snapshots at the final two steps to reconstruct the source wavefields backward in time. The checkpointing scheme was proposed by Griewank and Walther (2000) and applied to RTM by Symes (2007). Anderson et al. (2012) presented a modified checkpointing method, which saved a small number of full snapshots, needed to perform the crosscorrelation in RTM and FWI, to reduce the number of recomputations. The checkpointing method reduces the memory

usage but sacrifices the efficiency. By reconstructing the source wavefield in the forward-time direction, the checkpointing method is well suited for attenuating media (Yang et al., 2016). The classic boundary-value method reconstructs the source wavefield using saved wavefields at M layers of spatial grid points in the boundary (Gauthier et al., 1986; Dussaud et al., 2008) for a $(2M)$th accurate finite-difference (FD) operator. The classic method can achieve accurate reconstruction. However, the storage requirement is still tremendous for 3D models. To mitigate the problem, Feng and Wang (2012) presented a boundary-value method, which stores boundary wavefields at one layer of spatial grid points and reconstructs the source wavefield using the variable-order FD operators. Their method is of second-order accuracy in space. Tan and Huang (2014) saved boundary wavefields at one or two layers of grid points and reconstructed the source wavefield using a high-order wave-equation extrapolation method. The method can guarantee the accuracy and use 37.5% of the memory, required by the classic method of storing boundary wavefields at M layers of spatial grid points. Liu et al. (2015) proposed a new boundary-value method based on a linear combination of boundary wavefields. The storage amount of the method is $1/M$ of the classic method. The small degree of freedom leads to reduced accuracy, and the required number of sampling points per wavelength is approximately 5 to keep the error below 0.0025. For elastic FWI, Ren and Liu (2015) implemented wavefield reconstruction based on a combination of checkpointing and boundary-value methods. Raknes and Weibull (2016) presented an approximation boundary-value method, which only uses the particle velocity field in the boundary to reconstruct the source wavefield. One can avoid saving the source wavefield by using the random boundary condition (Clapp, 2009; Shen and Clapp, 2015). However, the coherent correlations may result in some artifacts in the shallow part of the model.

The boundary-value method is preferable to the checkpointing method because of its ability of balancing computational cost and storage amount, especially for lossless media. However, all of the existing boundary-value methods are based on explicit FD approximations of spatial derivatives. Compared with explicit methods, FD methods with an implicit space derivative operator need to solve tridiagonal matrix equations and thus require larger computational resources with the same operator length (Liu and Sen, 2009; Kosloff et al., 2010). As a result, implicit FD methods are rarely used in RTM and FWI. In fact, implicit FD operators yield greater accuracy than explicit ones with the same operator length (Chu and Stoffa, 2012; Liu, 2014; Wang and Liu, 2018; Wang et al., 2018; Ren and Li, 2019). Hence, we can improve the efficiency of RTM and FWI by using an implicit FD method with a smaller operator length for wavefield extrapolation. Note that the spatial derivatives in the inner and boundary areas are simultaneously obtained by solving matrix equations in implicit FD methods. The source wavefield in the inner area cannot be directly reconstructed using saved boundary wavefields. To solve the problem, we develop two boundary-value schemes, an accuracy-preserving scheme and a memory-efficient scheme, based on an implicit staggered-grid FD (SFD) operator. The former uses boundary wavefields at M layers of grid points and the spatial derivatives of wavefields at one layer of grid points to reconstruct the source wavefield for a $(2M + 2)$th accurate implicit SFD operator. The latter applies boundary wavefields at N layers of grid points, a linear combination of wavefields

at M−N layers of grid points, and the spatial derivatives of wavefields at one layer of grid points to reconstruct the source wavefield ($0 \leq N < M$). The required memory of the accuracy-preserving and memory-efficient schemes is $(M+1)/M$ and $(N+2)/M$ times, respectively, that of the explicit reconstruction scheme. Our work is a preliminary attempt to implicitly reconstruct the source wavefield, which can promote the application of advanced implicit FD methods in seismic imaging and inversion. The paper is organized as follows: first, we review an implicit SFD method; second, we introduce implicit source wavefield reconstruction schemes; third, we optimize the reconstruction coefficients; fourth, we analyze the accuracy and stability; finally, we apply the proposed reconstruction schemes to RTM on synthetic and field data.

2. Methodology

2.1. An implicit SFD method

The scalar wave equation is written as

$$\frac{\partial p}{\partial t} + K\nabla \cdot \mathbf{v} = 0 \quad \frac{\partial \mathbf{v}}{\partial t} + \frac{1}{\rho}\nabla p = 0 \tag{1}$$

where, $K = \rho v^2$, $\rho(x,y,z)$ is the density, $v(x,y,z)$ is the velocity, $p(x,y,z)$ is the pressure, and $\mathbf{v} = [v_x, v_y, v_z]^{\mathrm{T}}$ is the particle velocity vector. ∇ and $\nabla\cdot$ denote the gradient and divergence operator, respectively. The first-order spatial derivatives in Eq. (1) can be approximated by an implicit SFD operator (Liu and Sen, 2009; Liu, 2014). We have
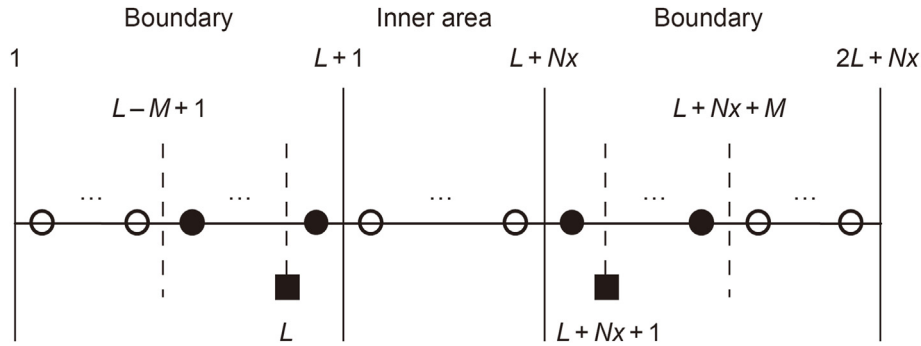
$$q(x-h) + aq(x) + q(x+h) \approx \frac{1}{h}\sum_{m=1}^{M} c_m[p(x+mh-0.5h) - p(x-mh+0.5h)] \tag{2}$$

where, h is the grid spacing, M is the operator length parameter, c_m and a are the FD coefficients, and $q = \frac{\partial p}{\partial x}$. We only show the formula for x-direction, and the derivatives along y- and z-directions are similarly computed. An absorbing boundary condition is generally needed to suppress the artificial reflections form the boundary. The spatial derivatives q in the inner and boundary areas are obtained by solving the tridiagonal matrix equation (Eq. (2)). Liu and Sen (2009) and Liu (2014) estimated FD coefficients based on the Taylor series expansion (TE) and least-squares (LS), respectively. They prove that an explicit SFD method can be replaced by an implicit SFD method with a smaller operator length, which increases the accuracy but not the computational cost. Additionally, the LS-based SFD method exhibits greater accuracy than the TE-based method with the same operator length. Here, we do not repeat the comparisons and focus on the source wavefield reconstruction based on implicit SFD methods.

2.2. Accuracy-preserving source wavefield reconstruction

For a model with the x-direction grid dimension of Nx and the number of boundary layers of L, Eq. (2) can be expressed as

$$\begin{bmatrix} a & 2 \\ 1 & a & 1 \\ & \ddots & \ddots & \ddots \\ & & 1 & a & 1 \\ & & & 1 & a & 1 \\ & & & & \ddots & \ddots & \ddots \\ & & & & & 1 & a & 1 \\ & & & & & & 1 & a & 1 \\ & & & & & & & \ddots & \ddots & \ddots \\ & & & & & & & & 1 & a & 1 \\ & & & & & & & & & 2 & a \end{bmatrix}$$

$$\times \begin{bmatrix} q_1 \\ q_2 \\ \vdots \\ q_L \\ q_{L+1} \\ \vdots \\ q_{L+Nx} \\ q_{L+Nx+1} \\ \vdots \\ q_{L+Nx+L-1} \\ q_{L+Nx+L} \end{bmatrix} = \begin{bmatrix} r_1 \\ r_2 \\ \vdots \\ r_L \\ r_{L+1} \\ \vdots \\ r_{L+Nx} \\ r_{L+Nx+1} \\ \vdots \\ r_{L+Nx+L-1} \\ r_{L+Nx+L} \end{bmatrix} \tag{3}$$

where,

$$r_i = \frac{1}{h} \sum_{m=1}^{M} c_m [p(ih + mh - 0.5h) - p(ih - mh + 0.5h)], \tag{4}$$
$$i = 1, 2, ..., 2L + Nx$$

We apply the mirror image method (Liu and Sen, 2009) to guarantee the accuracy of the derivatives near the boundary. Based on Eq. (3), a sub-equation (corresponding to the inner area) is derived

$$r_{L+M} = \frac{1}{h} \begin{bmatrix} \sum_{m=1}^{M-1} b_{M-1,m}[p((L+M+m-0.5)h) - p((L+M-m+0.5)h)] \\ + \sum_{m=1}^{N} b_{M-1,M-1+m}[p((L+2M+m-1.5)h) - p((L-m+1.5)h)] \\ + b_{M-1,M+N} \sum_{m=N+1}^{M} e_m[p((L+2M+m-1.5)h) - p((L-m+1.5)h)] \end{bmatrix} \tag{6}$$

$$\begin{bmatrix} a & 1 \\ 1 & a & 1 \\ & \ddots & \ddots & \ddots \\ & & 1 & a & 1 \\ & & & 1 & a \end{bmatrix} \begin{bmatrix} q_{L+1} \\ q_{L+2} \\ \vdots \\ q_{L+Nx-1} \\ q_{L+Nx} \end{bmatrix} = \begin{bmatrix} r_{L+1} - q_L \\ r_{L+2} \\ \vdots \\ r_{L+Nx-1} \\ r_{L+Nx} - q_{L+Nx+1} \end{bmatrix} \tag{5}$$

q_L and q_{L+Nx+1} are involved in the right side of Eq. (5), and boundary wavefields $p((L-m+1.5)h)$ and $p((L+Nx+m-0.5)h)$ ($m = 1, 2, ..., M$) are also needed to compute r_i ($i = L + 1, L + 2, ..., L + M, L + Nx - M + 1, L + Nx - M + 2, ..., L + Nx$). Fig. 1 shows a reconstruction stencil of our implicit scheme. Based on the stencil, we store $p((L - m + 1.5)h)$, $p((L + Nx + m - 0.5)h)$, q_L and q_{L+Nx+1} ($m = 1, 2, ..., M$) during the forward propagation and obtain the spatial derivatives q_i ($i = L + 1, L + 2, ..., L + Nx$) by solving Eq. (5) during the backward propagation. Likewise, we can compute the

spatial derivatives along y- and z-directions and further achieve the source wavefield reconstruction.

Note that the accuracy of our implicit reconstruction scheme is equal to that of the FD method used for wavefield extrapolation. For easy readability, we call the implicit scheme as the accuracy-preserving scheme. The classic explicit reconstruction scheme (Dussaud et al., 2008) only stores boundary wavefields at M layers of grid points. In contrast, the accuracy-preserving scheme needs to store both boundary wavefields at M layers of grid points ($p((L-m+1.5)h)$ and $p((L + Nx + m - 0.5)h)$, $m = 1, 2, ..., M$) and the spatial derivatives of wavefields at one layer of grid points (q_L and q_{L+Nx+1}). The memory usage of the accuracy-preserving scheme is $(M+1)/M$ times that of the explicit scheme.

2.3. Memory-efficient source wavefield reconstruction

The accuracy-preserving scheme is accurate but memory-expensive. To balance the accuracy and storage, we approximate r_i ($i = L + 1, L + 2, ..., L + M$) by

$$r_{L+1} = \frac{1}{h} \sum_{m=1}^{M} e_m[p((L+m+0.5)h) - p((L-m+1.5)h)]$$

$$r_{L+2} = \frac{1}{h} \begin{bmatrix} b_{1,1}[p((L+2.5)h) - p((L+1.5)h)] \\ + \sum_{m=1}^{N} b_{1,1+m}[p((L+m+2.5)h) - p((L-m+1.5)h)] \\ + b_{1,2+N} \sum_{m=N+1}^{M} e_m[p((L+m+2.5)h) - p((L-m+1.5)h)] \end{bmatrix}$$

where, N is a new operator length parameter ($0 \leq N < M$), e_m ($m = 1, 2, ..., M$) and $b_{l,m}$ ($l = 1, 2, ..., M - 1, m = 1, 2, ..., N + l + 1$) are the reconstruction coefficients. Eq. (6) is rewritten as

$$r_{L+1} = \frac{1}{h} \begin{bmatrix} \sum_{m=1}^{N} e_m[p((L+m+0.5)h) - p((L-m+1.5)h)] \\ + \sum_{m=N+1}^{M} e_m p((L+m+0.5)h) - A \end{bmatrix}$$

Fig. 1. The reconstruction stencil for the accuracy-preserving scheme. M is the operator length parameter, Nx is the x-direction grid dimension in the inner area, and L is the number of grid points in the boundary. We store the wavefields at M layers ($L - m + 1.5$ and $L + Nx + m − 0.5$, $m = 1, 2, \ldots, M$) (marked by filled circles) and the spatial derivatives of wavefields at one layer (L and $L + Nx +1$) (marked by squares), and use them to reconstruct the spatial derivatives between layers $L + 1$ and $L + Nx$. The wavefields marked by open circles are not stored.

$$r_{L+l}=\frac{1}{h}\left[\begin{array}{l}\sum_{m=1}^{l-1}b_{l-1,m}[p((L+l+m-0.5)h)-p((L+l-m+0.5)h)]\\[2mm]+\sum_{m=1}^{N}b_{l-1,l-1+m}[p((L+2l+m-1.5)h)-p((L-m+1.5)h)]\\[2mm]+b_{l-1,l+N}\sum_{m=N+1}^{M}e_m p((L+2l+m-1.5)h)-b_{l-1,l+N}A\end{array}\right] \tag{7}$$

where, $l = 2, 3, \ldots, M$, $A = \sum_{m=N+1}^{M}e_m p((L - m + 1.5)h)$.

r_i ($i = L + 1, L + 2, \ldots, L + M$) can be obtained as long as $p((L-m+1.5)h)$ ($m = 1, 2, \ldots, N$) and A are known in Eq. (7). Similarly, r_i ($i = L + Nx − M + 1, L + Nx − M + 2, \ldots, L + Nx$) are computed. q_L and q_{L+Nx+1} are also needed in the tridiagonal matrix equation (Eq. (5)). Using a new reconstruction stencil, illustrated in Fig. 2, we store boundary wavefields at M layers of grid points ($p((L -m +1.5)h)$ and $p((L + Nx + m − 0.5)h)$, $m = 1, 2, \ldots, N$), a linear combination of wavefields at $M−N$ layers of grid points (A), and the spatial derivatives of wavefields at one layer of grid points (q_L and q_{L+Nx+1}), and then reconstruct the spatial derivatives q_i ($i = L + 1, L + 2, \ldots, L + Nx$) based on Eqs. (5) and (7). The required memory is $(N+2)/M$ and $(N+2)/(M+1)$ times that of the explicit scheme and the accuracy-preserving scheme, respectively. This new implicit scheme is called as the memory-efficient scheme in the following sections.

Based on the plane wave assumption and Eqs. (2), (5) and (7)), we derive

$$\psi(k_x h) \approx \sum_{m=1}^{M} e_m \varphi_m(k_x h)$$

$$\psi(k_x h) \approx \sum_{m=1}^{l-1} b_{l-1,m}\varphi_m(k_x h) + \sum_{m=1}^{N} b_{l-1,l-1+m}\varphi_{l+m}(k_x h)$$

$$+ b_{l-1,l+N}\sum_{m=N+1}^{M} e_m \varphi_{l+m}(k_x h) \tag{8}$$

where,

$$\varphi_m(k_x h) = \sin((m-0.5)k_x h)\ \varphi_{l+m}(k_x h) = \sin((l+m-1.5)k_x h)$$

$$\psi(k_x h) = (a + 2\cos(k_x h))k_x h \,/\, 2 \tag{9}$$

$l = 2, 3, \ldots, M$, k_x is the wavenumber, and $k_x h$ equals π at the Nyquist frequency. Eq. (8) represents the dispersion relation of the memory-efficient scheme, and is used to estimate the reconstruction coefficients. The objective function is constructed as

$$f_1 = \int_0^{\beta_1} \left[\sum_{m=1}^{M} e_m \varphi_m(k_x h) - \psi(k_x h)\right]^2 dk_x h \tag{10}$$
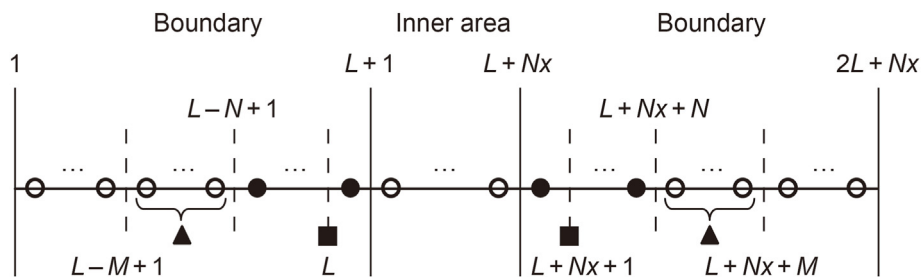
Fig. 2. The reconstruction stencil for the memory-efficient scheme. M and N are the operator length parameters, Nx is the x-direction grid dimension in the inner area, and L is the number of grid points in the boundary. We store the wavefields at N layers ($L - m + 1.5$ and $L + Nx + m − 0.5$, $m = 1, 2, \ldots, N$) (marked by filled circles), a linear combination of wavefields at $M − N$ layers ($L - m + 1.5$ and $L + Nx + m − 0.5$, $m = N + 1, N + 2, \ldots, M$) (marked by triangles), and the spatial derivatives of wavefields at one layer (L and $L + Nx +1$) (marked by squares), and use them to reconstruct the spatial derivatives between layers $L + 1$ and $L + Nx$. The wavefields marked by open circles are not stored.
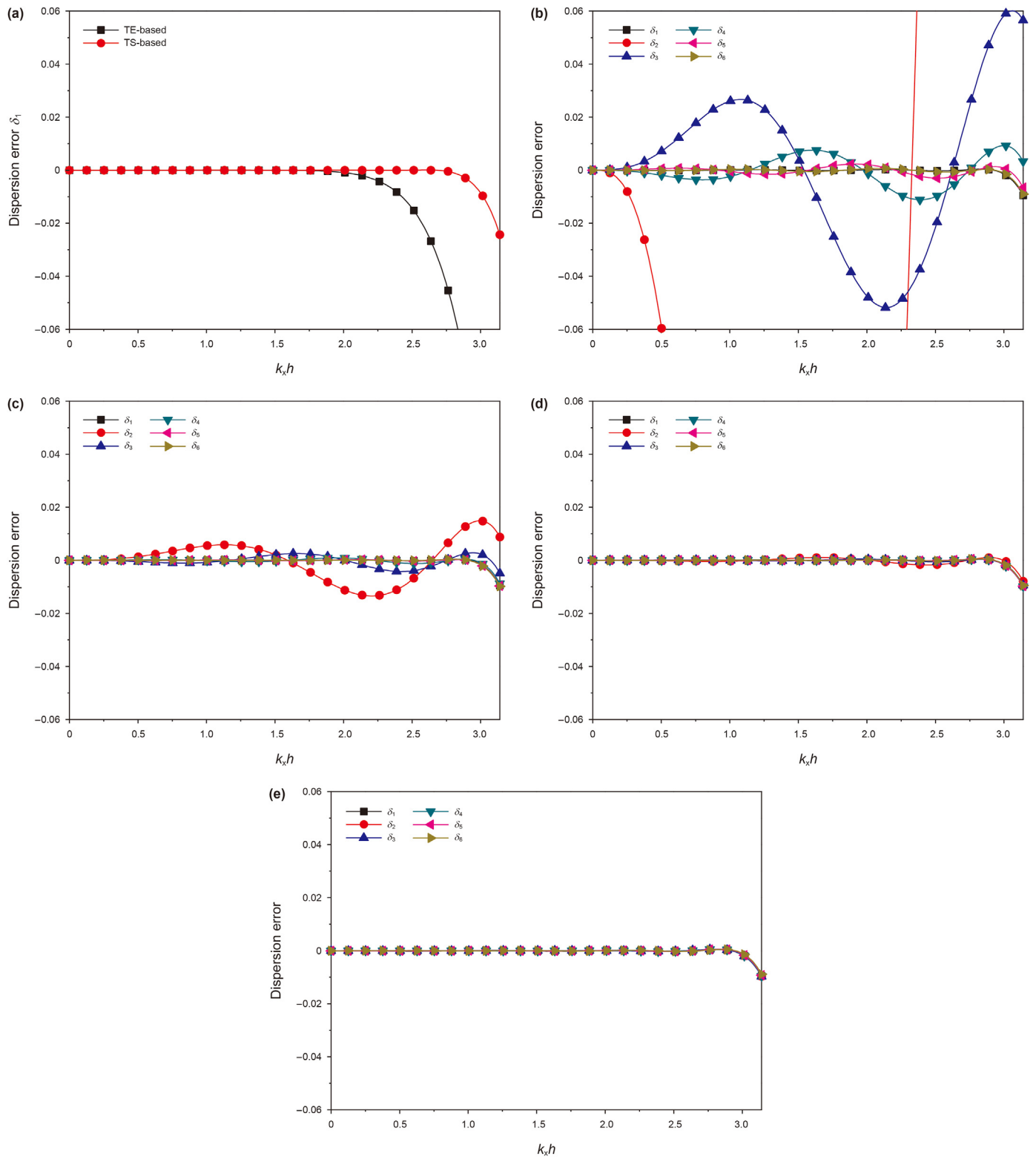
Fig. 3. The dispersion errors for different schemes with $M = 6$ and $\eta = 0.001$. (a) The accuracy-preserving scheme. The memory-efficient scheme with (b) $N = 0$, (c) $N = 1$, (d) $N = 2$ and (e) $N = 3$.

Table 1
The effective bandwidth β_f of different schemes with $\eta = 0.001$.

M	Accuracy-preserving scheme		Memory-efficient scheme			
	TE-based	LS-based	$N = 0$	$N = 1$	$N = 2$	$N = 3$
5	1.87	2.67	0.13	0.77	2.82	2.82
6	2.01	2.80	0.12	0.34	2.25	2.96
7	2.12	2.89	0.12	0.85	2.26	3.05

Table 2
The number of sampling points per wavelength G required by different schemes with $\eta = 0.001$.

M	Accuracy-preserving scheme		Memory-efficient scheme			
	TE-based	LS-based	$N = 0$	$N = 1$	$N = 2$	$N = 3$
5	3.36	2.35	48.33	8.16	2.23	2.23
6	3.13	2.24	52.36	18.48	2.79	2.12
7	2.96	2.17	52.36	7.39	2.78	2.06

Table 3
The stability factor s of different schemes with $\eta = 0.001$ for the 2D case.

M	Accuracy-preserving scheme		Memory-efficient scheme			
	TE-based	LS-based	$N = 0$	$N = 1$	$N = 2$	$N = 3$
5	0.5045	0.4784	0.1704	0.4616	0.4705	0.4694
6	0.4992	0.4730	0.1046	0.4375	0.4651	0.4642
7	0.4952	0.4691	0.0628	0.4047	0.4516	0.4594

$$f_l = \int_0^{\beta_l} \left[\sum_{m=1}^{l-1} b_{l-1,m}\varphi_m(k_xh) + \sum_{m=1}^{N} b_{l-1,l-1+m}\varphi_{l+m}(k_xh) + b_{l-1,l+N}\sum_{m=N+1}^{M} e_m\varphi_{l+m}(k_xh) - \psi(k_xh) \right]^2 \mathrm{d}k_xh$$

(11)

where, $l = 2, 3, \ldots, M$, β_1 and β_l are the upper limit of k_xh. To guarantee the accuracy at $k_xh = 0$, a constraint condition is needed (setting $k_xh = 0$ into Eq. (8))

$$\sum_{m=1}^{M} e_m(2m-1) = a + 2$$

(12)

$$\sum_{m=1}^{l-1} b_{l-1,m}(2m-1) + \sum_{m=1}^{N} b_{l-1,l-1+m}(2l+2m-3) + b_{l-1,l+N}\sum_{m=N+1}^{M} e_m(2l+2m-3) = a + 2$$

(13)

$l = 2, 3, \ldots, M$. Substituting Eqs. (12) and (13) into Eqs. (10) and (11) leads to

$$f_1 = \int_0^{\beta_1} \left[\sum_{m=1}^{M} e_m\xi_m(k_xh) + \lambda(k_xh) \right]^2 \mathrm{d}k_xh$$

(14)

$$f_l = \int_0^{\beta_l} \left[\sum_{m=1}^{l-1} b_{l-1,m}\zeta_m(k_xh) + \sum_{m=1}^{N} b_{l-1,l-1+m}\kappa_{l+m}(k_xh) + \mu(k_xh) \right]^2 \mathrm{d}k_xh$$

(15)

$$\xi_m(k_xh) = \varphi_m(k_xh) - (m - 0.5)k_xh \quad \zeta_m(k_xh) = \varphi_m(k_xh) - (2m-1)X/Q$$

$$\kappa_{l+m}(k_xh) = \varphi_{l+m}(k_xh) - (2l+2m-3)X/Q$$

$$\lambda(k_xh) = (1 - \cos(k_xh))k_xh \quad \mu(k_xh) = (a+2)X/Q - (a+2\cos(k_xh))k_xh/2$$

Table 4
The reconstruction coefficients of the memory-efficient scheme with $N = 1$, $M = 6$ and $\eta = 0.001$.

Coefficients	i						
	1	2	3	4	5	6	7
a_i	1.37322163	1.01477876	−0.05638370	0.01014384	−0.00255088	0.00057296	–
$b_{1,i}$	1.37329842	1.01445218	−0.04771983	–	–	–	–
$b_{2,i}$	1.37323846	1.01483479	−0.05629359	0.00803770	–	−0.00198610	–
$b_{3,i}$	1.37317612	1.01483696	−0.05641441	0.01021264	−0.00256029	0.00055782	–
$b_{4,i}$	1.37317634	1.01483884	−0.05641206	0.01021663	−0.00252617	0.00066087	–
$b_{5,i}$	1.37319693	1.01482596	−0.05638440	0.01021206	−0.00252617	0.00066087	−0.00014262

Table 5
The reconstruction coefficients of the memory-efficient scheme with $N = 2$, $M = 6$ and $\eta = 0.001$.

Coefficients	i							
	1	2	3	4	5	6	7	8
a_i	1.37322163	1.01477876	−0.05638370	0.01014384	−0.00255088	0.00057296	–	–
$b_{1,i}$	1.37320279	1.01483194	−0.05636734	−0.16706353	–	–	–	–
$b_{2,i}$	1.37318547	1.01483616	−0.05639732	0.01022119	0.04106361	–	–	–
$b_{3,i}$	1.37319444	1.01481875	−0.05639714	0.01019569	−0.00254965	−0.01142050	–	–
$b_{4,i}$	1.37321962	1.01480434	−0.05636187	0.01019273	−0.00250495	0.00064491	0.00282222	–
$b_{5,i}$	1.37324463	1.01477107	−0.05634593	0.01015199	−0.00249886	0.00059747	−0.00008211	−0.00011800

(a) Distance, m

(b) Distance, m
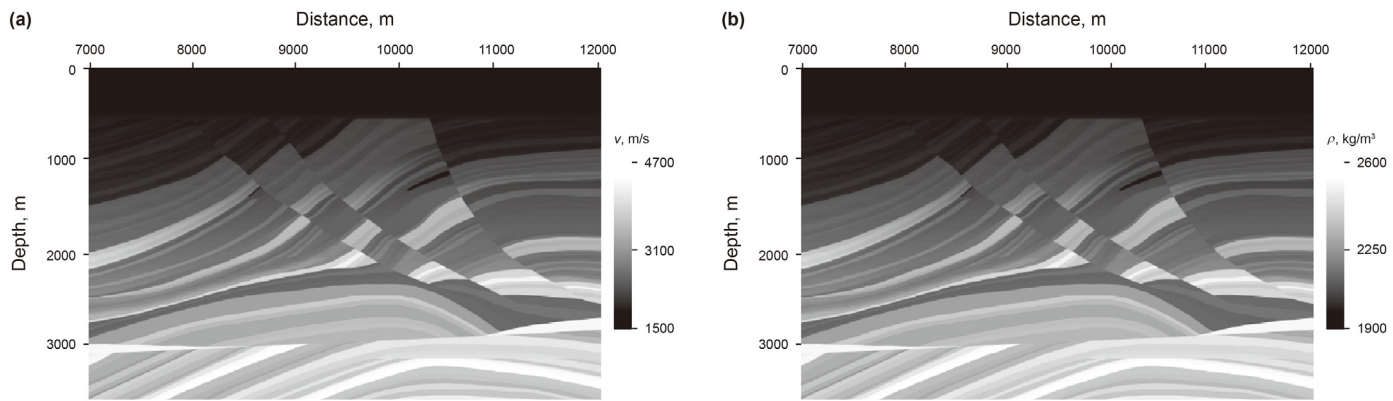
Fig. 4. The acoustic Marmousi model. (a) Velocity. (b) Density.
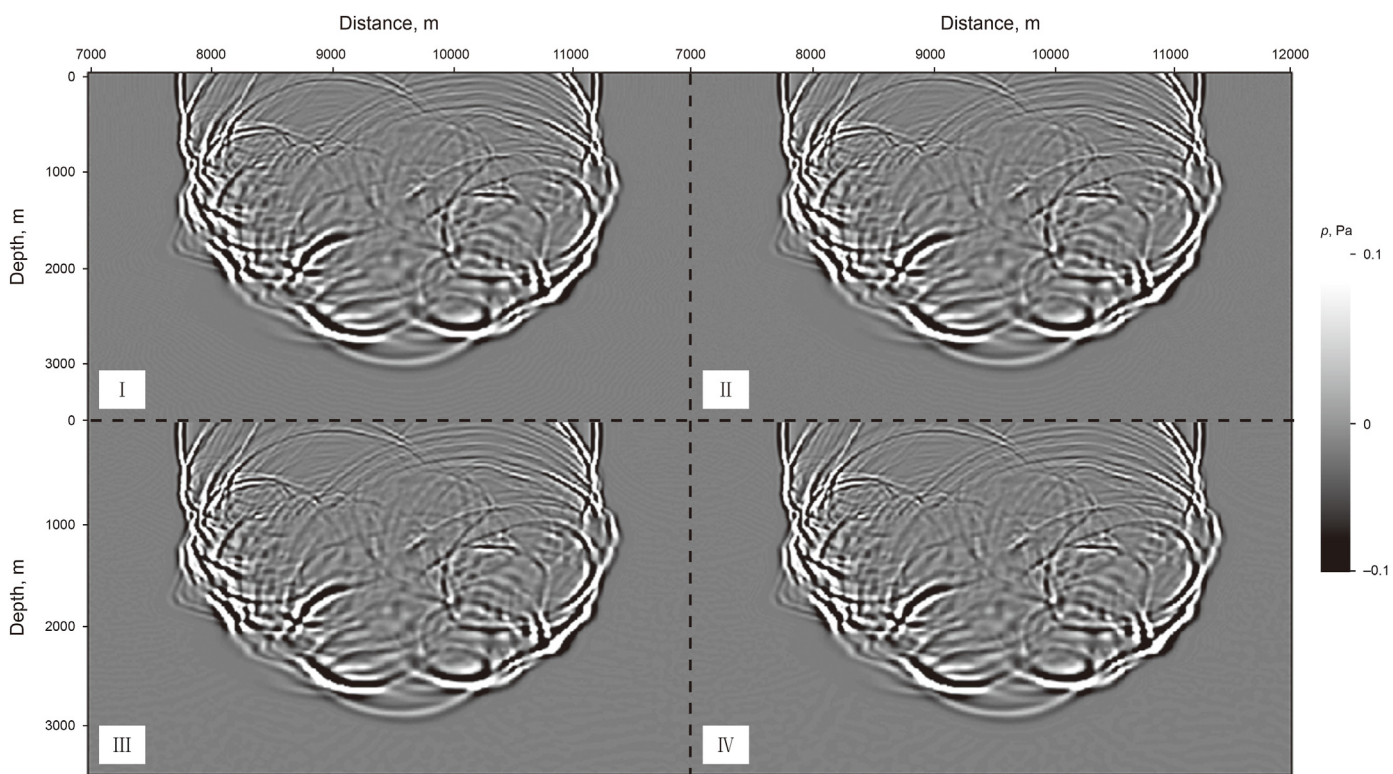

Distance, m   Distance, m

Fig. 5. The snapshots at 1.2 s reconstructed by different schemes for the Marmousi model. Panel I shows the forward source wavefield, and panels II, III and IV are for the accuracy-preserving scheme, the memory-efficient scheme with $N = 1$ and $N = 2$, respectively.
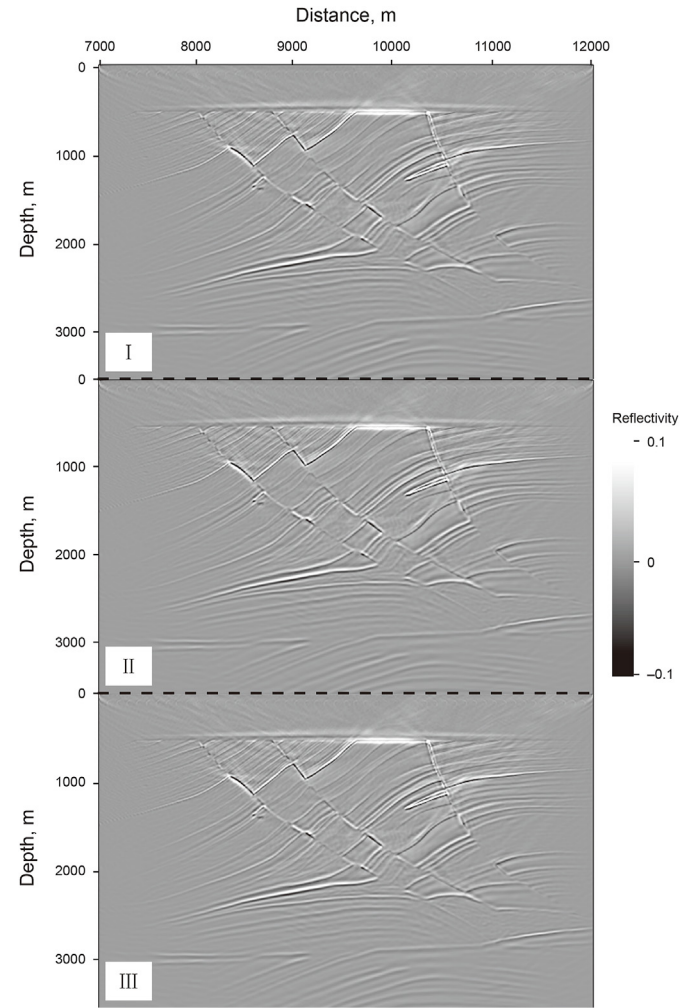
$$Q = \sum_{m=N+1}^{M} e_m (2l + 2m - 3) \quad X = \sum_{m=N+1}^{M} e_m \varphi_{l+m}(k_x h) \tag{16}$$

$l = 2, 3, \ldots, M.$

The minimization problem (Eqs. (14) and (15)) is solved by LS, and we have

$$\frac{\partial f_1}{e_n} = \sum_{m=1}^{M} e_m \int_0^{\beta_1} \xi_m(k_x h) \xi_n(k_x h) \mathrm{d}k_x h + \int_0^{\beta_1} \lambda(k_x h) \xi_n(k_x h) \mathrm{d}k_x h = 0 \tag{17}$$

$n = 1, 2, \ldots, M,$

$$\frac{\partial f_l}{b_{l-1,n}} = \sum_{m=1}^{l-1} b_{l-1,m} \int_0^{\beta_l} \zeta_m(k_x h) \zeta_n(k_x h) \mathrm{d}k_x h + \sum_{m=1}^{N} b_{l-1,l-1+m} \int_0^{\beta_l} \kappa_{l+m}(k_x h) \zeta_n(k_x h) \mathrm{d}k_x h + \int_0^{\beta_l} \mu(k_x h) \zeta_n(k_x h) \mathrm{d}k_x h = 0 \tag{18}$$
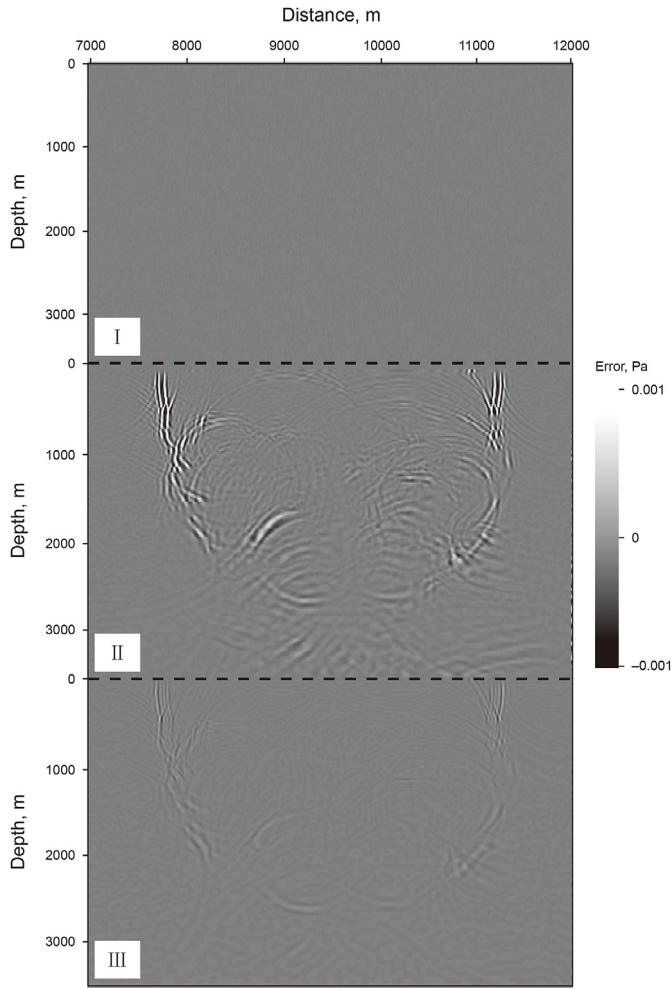
Fig. 6. The difference between the forward source wavefield and the wavefields reconstructed by different schemes for the Marmousi model. Panels I, II and III are for the accuracy-preserving scheme, the memory-efficient scheme with $N = 1$ and $N = 2$, respectively.

Fig. 7. The RTM images of different schemes for the Marmousi model. Panels I, II and III are for the accuracy-preserving scheme, the memory-efficient scheme with $N = 1$ and $N = 2$, respectively.

Table 6
The maximum absolute value ε_{MAV} and root mean square ε_{RMS} errors of reconstructed wavefields for the Marmousi model.

Schemes	ε_{MAV}	ε_{RMS}
Accuracy-preserving scheme	0.00000255	0.00000021
Memory-efficient scheme with $N = 1$	0.00789540	0.00014405
Memory-efficient scheme with $N = 2$	0.00164897	0.00002434

$$n = 1, 2, \ldots, l - 1,$$

(1) For the given operator length (M and N), allowed error limit (η) and maximum wavenumber (β_1), obtain e_m ($m = 1, 2, \ldots M$) by solving the linear equations (Eq. (17));

(2) Compute a using e_m ($m = 1, 2, \ldots M$) and the constraint condition (Eq. (12));

(3) Estimate the maximum error E_1 by

$$E_1 = \max_{k_x h \in [0, \beta_1]} |\delta_1(k_x h)| \tag{20}$$

$$\frac{\partial f_l}{b_{l-1, l-1+n}} = \sum_{m=1}^{l-1} b_{l-1, m} \int_0^{\beta_l} \zeta_m(k_x h) \kappa_{l+n}(k_x h) \mathrm{d}k_x h + \sum_{m=1}^{N} b_{l-1, l-1+m} \int_0^{\beta_l} \kappa_{l+m}(k_x h) \kappa_{l+n}(k_x h) \mathrm{d}k_x h + \int_0^{\beta_l} \mu(k_x h) \kappa_{l+n}(k_x h) \mathrm{d}k_x h = 0 \tag{19}$$

where,

$$n = 1, 2, \ldots, N, \text{ and } l = 2, 3, \ldots, M.$$
The detailed steps of calculating the coefficients are as follows:

$$\delta_1(k_x h) = \sum_{m=1}^{M} e_m \varphi_m(k_x h) - \psi(k_x h) \tag{21}$$
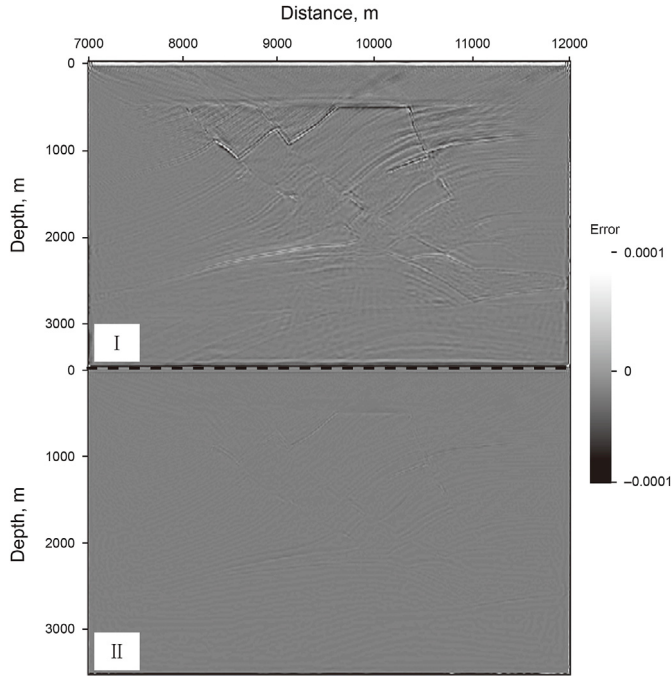
Fig. 8. The difference between the images of the accuracy-preserving scheme and the memory-efficient scheme for the Marmousi model. Panels I and II are for $N = 1$ and $N = 2$, respectively.

Table 7
The maximum absolute value ε_{MAV} and root mean square ε_{RMS} errors of images for the Marmousi model.

| Schemes	ε_{MAV}	ε_{RMS}
Memory-efficient scheme with $N = 1$	0.15320323	0.00080112
Memory-efficient scheme with $N = 2$	0.00384442	0.00007477

If $E_1 > \eta$, decrease β_1 and return to step 1. Otherwise, output e_m ($m = 1, 2, \ldots M$), a and β_1;

(4) For the allowed error limit (η) and maximum wavenumber β_l ($l = 2, 3, \ldots, M$), get $b_{l-1,m}$ ($l = 2, 3, \ldots, M, m = 1, 2, \ldots, l-1+N$) by solving the linear equations (Eqs. (18) and (19));

(5) Calculate $b_{l-1,l+N}$ using $b_{l-1,m}$ ($l = 2, 3, \ldots, M, m = 1, 2, \ldots, l-1+N$) and the constraint condition (Eq. (13));

(6) Estimate the maximum error E_l by
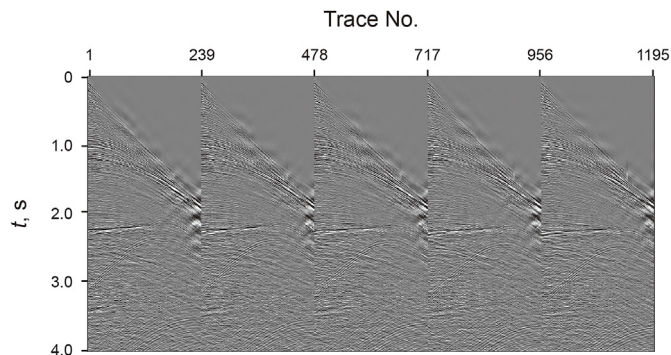
Fig. 9. The first five shot gathers for the field data example.
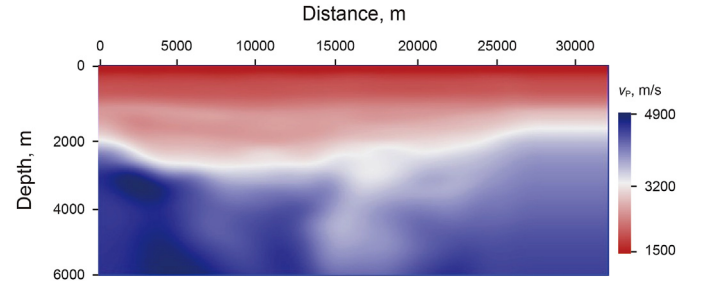
Fig. 10. The velocity model for the field data example.

$$E_l = \max_{k_x h \in [0, \beta_l]} |\delta_l(k_x h)| \tag{22}$$

where,

$$\delta_l(k_x h) = \sum_{m=1}^{l-1} b_{l-1,m} \varphi_m(k_x h) + \sum_{m=1}^{N} b_{l-1,l-1+m} \varphi_{l+m}(k_x h) + b_{l-1,l+N} \sum_{m=N+1}^{M} e_m \varphi_{l+m}(k_x h) - \psi(k_x h) \tag{23}$$

($l = 2, 3, \ldots, M$). If $E_l > \eta$, decrease β_l and return to step 4. Otherwise, output $b_{l,m}$ ($l = 1, 2, \ldots, M-1, m = 1, 2, \ldots, N+l+1$) and β_l ($l = 2, 3, \ldots, M$).

We obtain the optimized reconstruction coefficients and wavenumber range β_l ($l = 1, 2, \ldots, M$). The effective bandwidth of the memory-efficient scheme is determined by

$$\beta_f = \min_{j=1,2,\ldots,M} \beta_l \tag{24}$$

Eqs. (21) and (23) denote the absolute error of both sides in the dispersion relation (Eq. (8)), and can be used to evaluate the accuracy of the reconstruction scheme. The optimization process ensures that the dispersion of the memory-efficient scheme is less than the allowed error limit η within $[0, \beta_f]$.

The FD coefficients, based on TE (Liu and Sen, 2009) or LS (Liu, 2014), are used as the reconstruction coefficients in the accuracy-preserving scheme. We can analyze its accuracy by replacing e_m with c_m ($m = 1, 2, \ldots M$) in Eqs. (20) and (21), and estimate its effective bandwidth by setting $E_1 \leq \eta$.

2.4. Accuracy and stability analyses

Fig. 3 shows the dispersion curves of different schemes. It is observed that the accuracy-preserving scheme with TE-based coefficients produces strong dispersion in the high-wavenumber zone. These dispersion can be effectively suppressed by using LS-based coefficients. When $N = 0$, the memory-efficient scheme obtains inaccurate results, especially for δ_2 at the layer of $x = (L + 2)h$. The accuracy is significantly improved with N increasing, and the dispersion becomes invisible for $N = 2$. Table 1 displays the bandwidth (β_f) of different schemes. The accuracy-preserving scheme with LS-based coefficients yields larger β_f compared to the scheme with TE-based coefficients. The bandwidth of the memory-efficient scheme increases with N, and $N = 2$ can ensure that the error is less than 0.001 within a large β_f (more than 2.2). We transform the bandwidth into the number of sampling points per wavelength (G) by $G = 2\pi/\beta_f$. Table 2 shows G for different schemes. The accuracy-preserving scheme with LS-based coefficients and the memory-efficient scheme ($N = 2$) require smaller G (less than 3) to keep the dispersion below the error limit $\eta = 0.001$. Additionally, the

(a)

(b)

(c)
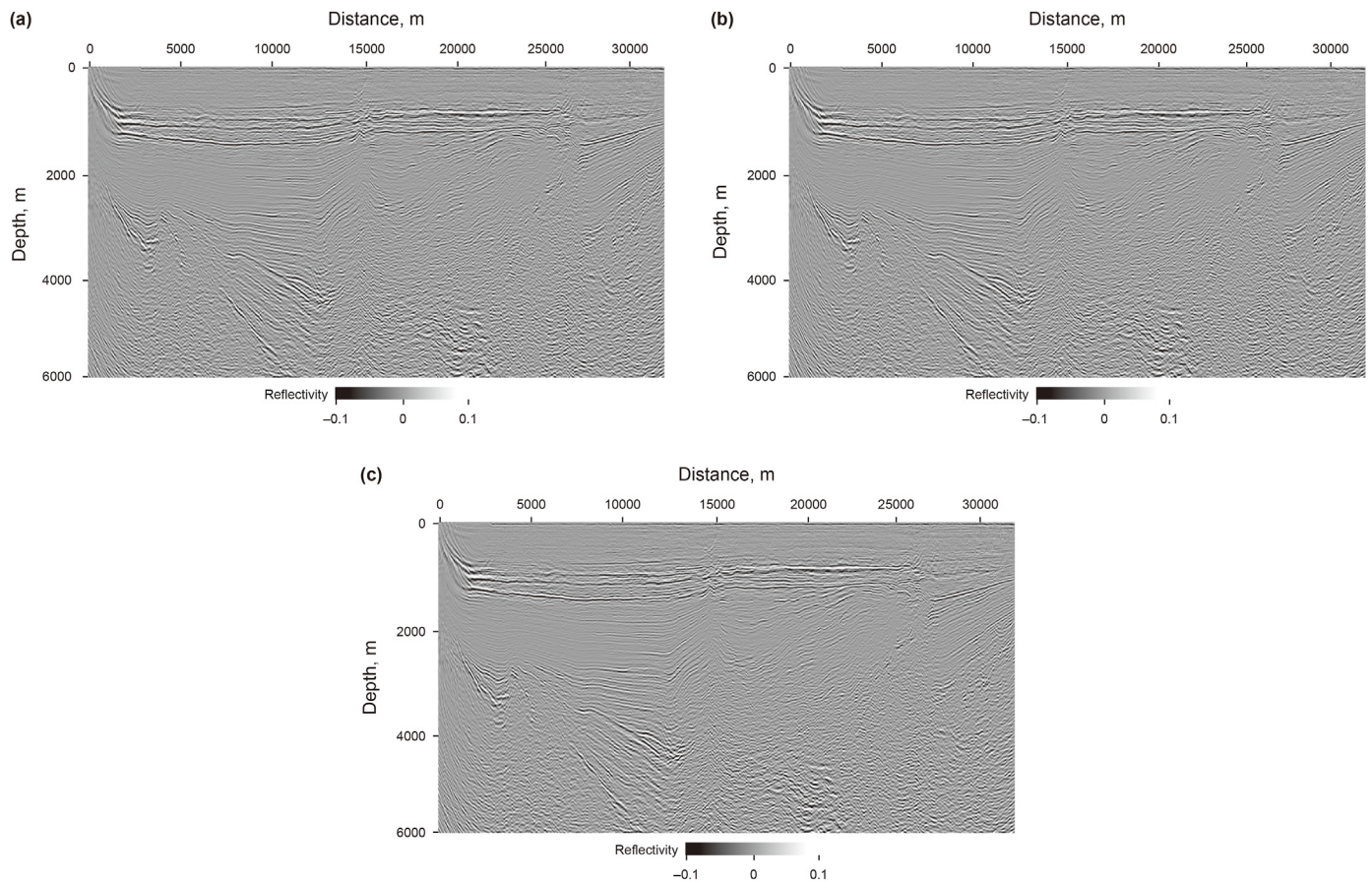
Fig. 11. The RTM images of different schemes for the field data example. (a), (b) and (c) are for the accuracy-preserving scheme, the memory-efficient scheme with $N = 1$ and $N = 2$, respectively.

required number of sampling points per wavelength decreases with N increasing for the memory-efficient scheme.

We derive the stability condition of the proposed schemes based on the standard von Neumann analysis (Chen, 2011; Wang and Liu, 2018; Ren and Li, 2019). The stability factor for the 2D case is

$$s = \min_{l=1,2,\ldots,M} s_l \tag{25}$$

where,

$$s_1 = \frac{\sqrt{2}(a-2)}{2}\left(\sum_{m=1}^{M} e_m(-1)^{m+1}\right)^{-1} \tag{26}$$

$$s_l = \frac{\sqrt{2}(a-2)}{2}\left(\begin{array}{c}\sum_{m=1}^{l-1} b_{l-1,m}(-1)^{m+1} + \sum_{m=1}^{N} b_{l-1,l-1+m}(-1)^{l+m} \\ + b_{l-1,l+N}\sum_{m=N+1}^{M} e_m(-1)^{l+m}\end{array}\right)^{-1} \tag{27}$$

$j = 2, 3, \ldots, M$. The reconstruction schemes are stable when the maximum Courant number is less than s. Table 3 shows s for different schemes, and the factor for the 3D case is $\sqrt{2/3}s$. The accuracy-preserving scheme with LS-based coefficients exhibits slightly stricter stability condition compared to the scheme with TE-based coefficients. The stability of the memory-efficient scheme becomes better with N increasing, and the value of s is more than

0.4 for $N \geq 1$. We do not use the memory-efficient scheme with $N = 0$ because of its poor stability.

3. Examples

We apply the proposed reconstruction schemes to RTM on
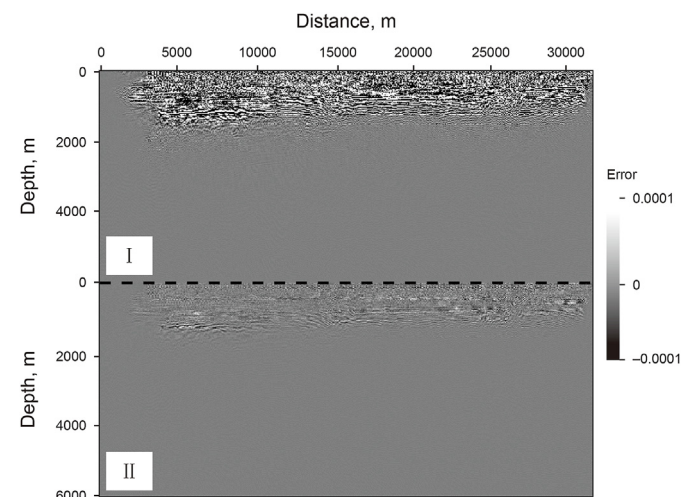
Fig. 12. The difference between the images of the accuracy-preserving scheme and the memory-efficient scheme for the field data example. Panels I and II are for $N = 1$ and $N = 2$, respectively.

Table 8
The maximum absolute value ε_{MAV} and root mean square ε_{RMS} errors of images for the field data example.

Schemes	ε_{MAV}	ε_{RMS}
Memory-efficient scheme with $N = 1$	0.03456935	0.00156818
Memory-efficient scheme with $N = 2$	0.00280413	0.00014942

Table 9
The storage amount of different schemes for the field data.

Schemes	Storage amount (GB)
Storing the source wavefield without reconstruction	56.90
Accuracy-preserving scheme	1.90
Memory-efficient scheme with $N = 1$	0.54
Memory-efficient scheme with $N = 2$	0.82

synthetic and field data. The LS-based implicit SFD method (Liu, 2014) with $M = 6$ is used for modeling of the variable-density acoustic wave equation. The codes are executed on an personal workstation (HP Z820 E5−2640 with two quad-core Intel Xeon 2.5 GHz processors and 32 GB of memory). The LS-based FD coefficients (Liu, 2014) are directly used as the reconstruction coefficients in the accuracy-preserving scheme. The reconstruction coefficients of the memory-efficient scheme with $N = 1$ and 2 are shown in Tables 4 and 5, and $a = 2.18999094$.

3.1. Marmousi model example

The first example is for the Marmousi model, shown in Fig. 4. The grid spacing is 10 m, the grid dimensions are 351×501, the time step is 0.8 ms, and the maximum recording time is 3.2 s. The source signal is represented by a Ricker wavelet with a peak frequency of 20 Hz. 51 sources and 501 receivers are evenly distributed on the surface. Fig. 5 displays the snapshots reconstructed by different schemes. Fig. 6 illustrates the subtraction of the reconstructed wavefields and the forward-propagated source wavefield (used as a reference). We observe that the snapshot reconstructed by the accuracy-preserving scheme is in good agreement with the reference solution and the difference between them is negligible. For the memory-efficient scheme, the reconstruction accuracy is improved with N increasing. Table 6 shows the maximum absolute value (ε_{MAV}) and root mean square (ε_{RMS}) errors (relative to the reference) for different schemes. Note that the forward-propagated and reconstructed wavefields are normalized and thus the errors are dimensionless. The accuracy-preserving scheme is sufficiently accurate and ε_{MAV} is on the order of 10^{-6} (single-precision floating point number). In contrast, ε_{MAV} and ε_{RMS} for the memory-efficient scheme with $N = 2$ are on the order of 10^{-3} and 10^{-5}, respectively. Fig. 7 displays the RTM images for different schemes. We illustrates the difference between images of the accuracy-preserving scheme (used as a reference) and the memory-efficient scheme with different N in Fig. 8. It is seen that the image for $N = 2$ is much closer to the reference solution compared to the image for $N = 1$. Table 7 shows ε_{MAV} and ε_{RMS} of images for the memory-efficient scheme. To make a fair comparison, the images for different schemes are normalized. The errors become smaller as N increases and the maximum absolute value error for $N = 2$ is on the order of 10^{-3}, which is sufficient for high-accuracy imaging. Meanwhile, the memory-efficient scheme with $N = 2$ only uses 57% of the memory, required by the accuracy-preserving scheme.

3.2. Field data example

We prove the effectiveness of the proposed schemes using a real offshore data set, containing 574 shot gathers with a source interval of 50 m. There are 239 traces with a trace interval of 12.5 m for each shot gather. Fig. 9 illustrates the first five shot gathers. The velocity model is shown in Fig. 10, and the density model is computed by Gardner's equation (Gardner et al., 1974). The grid dimensions are 2540×501, the grid spacing is 12.5 m, the time step is 1.0 ms, and the maximum recording time is 4.0 s. A minimum-phase wavelet, extracted by a commercial software, is used as a source. Fig. 11 displays the RTM images for different schemes. It is observed that either the accuracy-preserving scheme or the memory-efficient scheme can obtain plausible results, and the main reflection events are continuous. We also use the image for the accuracy-preserving scheme as a reference solution to evaluate the accuracy of the memory-efficient scheme with different N. Fig. 12 depicts the difference between the image of the memory-efficient scheme and the reference solution. The image for $N = 1$ marginally deviates from the reference solution, especially for shallow depths. This problem can be significantly mitigated by using a larger N. Table 8 shows the maximum absolute value and root mean square errors of the normalized images for the memory-efficient scheme. The errors gradually decrease with N increasing, and ε_{MAV} and ε_{RMS} for $N = 2$ on the order of 10^{-3} and 10^{-4}, respectively. The memory usage of the memory-efficient scheme with $N = 2$ is only $4/(M+1)$ times that of the accuracy-preserving scheme. Hence, the memory-efficient scheme can guarantee the reconstruction accuracy with a modest storage cost.

Table 9 shows the memory usage of different schemes. In this example, the storage requirements of the source wavefield without reconstruction are $2540 \times 501 \times 4001 \times 4$ (single-precision floating point) $\times 3$ (the acoustic velocity-stress equation)$/1024^3 = 56.90$ GB. The memory required by the accuracy-preserving scheme becomes $(2540 + 501) \times 2 \times 4001 \times 7 \times 4 \times 3/1024^3 = 1.90$ GB. The storage amount is reduced to 0.54 or 0.82 GB by using the memory-efficient scheme with $N = 1$ or 2. The proposed schemes can be directly applied to the 3D case. For a large-scale 3D model, one can combine the proposed schemes with the checkpointing method to further mitigate the storage burden.

The runtime becomes different for different schemes and N in the computation of r_i ($i = L + 1, L + 2, ..., L + M$) (Eqs. (4) and (7)). We can analyze their efficiency by comparing the number of floating-point operations in Eqs. (4) and (7), which is $3M^2$ and $(7M^2+2MN+3M-4)/2$ respectively. The memory-efficient scheme is slightly more expensive than the accuracy-preserving scheme. However, the additional computation is very small compared to forward modeling.

4. Conclusions

We develop two source wavefield reconstruction schemes, an accuracy-preserving scheme and a memory-efficient scheme. Based on new implicit reconstruction stencils, the former uses boundary wavefields at M layers of spatial grid points and the spatial derivatives of wavefields at one layer of spatial grid points to reconstruct the source wavefield; the latter applies boundary wavefields at N layers of spatial grid points, a linear combination of wavefields at $M−N$ layers of spatial grid points, and the spatial derivatives of wavefields at one layer of spatial grid points to reconstruct the source wavefield (M and N are the operator length parameters, $0 \leq N < M$). The memory usage of the accuracy-preserving and memory-efficient schemes is $(M+1)/M$ and $(N+2)/M$ times, respectively, that of the classic reconstruction scheme based on the explicit FD operator. The accuracy-preserving scheme

exhibits higher reconstruction accuracy but requires larger computer memory, whereas the memory-efficient scheme with $N = 2$ can balance the accuracy and storage.

We test the implicit reconstruction schemes on acoustic RTM. The schemes are applicable for elastic RTM and other geophysical problems based on the adjoint-state method, such as FWI and LS RTM. It is straightforward to develop source wavefield reconstruction schemes for implicit centered-grid FD operators. Our schemes suffer from instability problem in attenuating media, and thus cannot be directly used for viscoacoustic or viscoelastic imaging and inversion.

Acknowledgments

References

Anderson, J.E., Tan, L., Wang, D., 2012. Time-reversal checkpointing methods for RTM and FWI. Geophysics 77 (4), S93–S103. https://doi.org/10.1190/GEO2011-0114.1.

Chen, J., 2011. A stability formula for Lax-Wendroff methods with fourth-order in time and general-order in space for the scalar wave equation. Geophysics 76 (5), T37–T42. https://doi.org/10.1190/1.3554626.

Chu, C., Stoffa, P.L., 2012. An implicit finite-difference operator for the Helmholtz equation. Geophysics 77 (4), T97–T107. https://doi.org/10.1190/geo2011-0314.1.

Clapp, R., 2009. Reverse time migration with random boundaries. 79th Ann. Int. Meet. SEG, Expand. Abstr. 2809–2813. https://doi.org/10.1190/1.3255432.

Dussaud, E., Symes, W., Williamson, P., et al., 2008. Computational strategies for reverse-time migration. 78th Ann. Int. Meet. SEG, Expand. Abstr. 2267–2271. https://doi.org/10.1190/1.3059336.

Feng, B., Wang, H., 2012. Reverse time migration with source wavefield reconstruction strategy. J. Geophys. Eng. 9, 69–74. https://doi.org/10.1088/1742-2132/9/1/008.

Gardner, G., Gardner, L.W., Gregory, A.R., 1974. Formation velocity and density; the diagnostic basics for stratigraphic traps. Geophysics 39 (6), 770–780. https://doi.org/10.1190/1.1440465.

Gauthier, O., Virieux, J., Tarantola, A., 1986. Two-dimensional nonlinear inversion of seismic waveforms: numerical results. Geophysics 51 (7), 1387–1403. https://doi.org/10.1190/1.1442188.

Griewank, A., Walther, A., 2000. Algorithm 799: an implementation of checkpointing for the reverse or adjoint mode of computational differentiation. ACM Trans. Math Software. 26 (1), 19–45. https://doi.org/10.1145/347837.347846.

Gu, B., Ren, Z., Li, Q., et al., 2019. An application of vector wavefield decomposition to 3D elastic reverse time migration and field data test. Comput. Geosci.-UK. 131, 112–131. https://doi.org/10.1016/j.cageo.2019.07.001.

Kosloff, D., Pestana, R.C., Tal-Ezer, H., 2010. Acoustic and elastic numerical wave simulations by recursive spatial derivative operators. Geophysics 75 (6), T167–T174. https://doi.org/10.1190/1.3485217.

Liu, F., Zhang, G., Morton, S.A., et al., 2011. An effective imaging condition for reverse-time migration using wavefield decomposition. Geophysics 76 (1), S29–S39. https://doi.org/10.1190/1.3533914.

Liu, S., Li, X., Wang, W., et al., 2015. Source wavefield reconstruction using a linear combination of the boundary wavefield in reverse time migration. Geophysics 80 (6), S203–S212. https://doi.org/10.1190/geo2015-0109.1.

Liu, Y., 2014. Optimal staggered-grid finite-difference schemes based on least-squares for wave equation modeling. Geophys. J. Int. 197 (2), 1033–1047. https://doi.org/10.1093/gji/ggu032.

Liu, Y., Sen, 2009. An implicit staggered-grid finite-difference method for seismic modeling. Geophys. J. Int. 179 (1), 459–474. https://doi.org/10.1111/j.1365-246X.2009.04305.x.

McMechan, G., 1983. Migration by extrapolation of time-dependent boundary values. Geophys. Prospect. 31 (3), 413–420. https://doi.org/10.1111/j.1365-2478.1983.tb01060.x.

Métivier, L., Brossier, R., Mérigot, Q., et al., 2017. Measuring the misfit between seismograms using an optimal transport distance: application to full waveform inversion. Geophys. J. Int. 205 (1), 345–377. https://doi.org/10.1093/gji/ggw014.

Plessix, R.E., 2006. A review of the adjoint-state method for computing the gradient of a functional with geophysical applications. Geophys. J. Int. 167 (2), 495–503. https://doi.org/10.1111/j.1365-246X.2006.02978.x.

Raknes, E.B., Weibull, W., 2016. Efficient 3D elastic full-waveform inversion using wavefield reconstruction methods. Geophysics 81 (2), R45–R55. https://doi.org/10.1190/geo2015-0185.1.

Ren, Z., Liu, Y., 2015. Elastic full-waveform inversion using the second-generation wavelet and an adaptive-operator-length scheme. Geophysics 80 (4), R155–R173. https://doi.org/10.1190/geo2014-0516.1.

Ren, Z., Li, Z., 2019. High-order temporal and implicit spatial staggered-grid finite-difference operators for modelling seismic wave propagation. Geophys. J. Int. 217 (2), 844–865. https://doi.org/10.1093/gji/ggz059.

Shen, X., Clapp, R.G., 2015. Random boundary condition for memory-efficient waveform inversion gradient computation. Geophysics 80 (6), R351–R359. https://doi.org/10.1190/geo2014-0542.1.

Symes, W.W., 2007. Reverse time migration with optimal checkpointing. Geophysics 72 (5), SM213–SM221. https://doi.org/10.1190/1.2742686.

Tan, S., Huang, L., 2014. Reducing the computer memory requirement for 3D reverse-time migration with a boundary-wavefield extrapolation method. Geophysics 79 (5), S185–S194. https://doi.org/10.1190/geo2014-0075.1.

Tarantola, A., 1984. Inversion of seismic reflection data in the acoustic approximation. Geophysics 49 (8), 1259–1266. https://doi.org/10.1190/1.1441754.

Virieux, J., Operto, S., 2009. An overview of full-waveform inversion in exploration geophysics. Geophysics 74 (6), WCC1–WCC26. https://doi.org/10.1190/1.3238367.

Wang, E., Liu, Y., 2018. An implicit spatial and high-order temporal finite difference scheme for 2D acoustic modeling. Explor. Geophys. 49, 187–201. https://doi.org/10.1071/EG16094.

Wang, E., Ba, J., Liu, Y., 2018. Time-space-domain implicit finite difference methods for modeling acoustic wave equations. Geophysics 83 (4), T175–T193. https://doi.org/10.1190/geo2017-0546.1.

Yang, P., Brossier, R., Métivier, L., et al., 2016. Wavefield reconstruction in attenuating media: a checkpointing-assisted reverse-forward simulation method. Geophysics 81 (6), R349–R362. https://doi.org/10.1190/geo2016-0082.1.

Zhang, Y., Sun, J., Gray, S., 2007. Reverse-time migration: Amplitude and implementation issues. 77th Ann. Int. Meet. SEG, Expand. Abstr. 2145–2149. https://doi.org/10.1190/1.2792912.

Zhang, Z., Alkhalifah, T., 2019. Regularized elastic full-waveform inversion using deep learning. Geophysics 84 (5), R741–R751. https://doi.org/10.1190/geo2018-0685.1.